*Manuscript

Original Manuscript

FINITE ELEMENT PREDICTION OF SURFACE STRAIN AND FRACTURE STRENGTH AT THE DISTAL RADIUS

W. Brent Edwards [a], Karen L. Troy [ab]

a Department of Kinesiology and Nutrition

b Department of Bioengineering

University of Illinois at Chicago,

Chicago, IL 60612, USA

Corresponding Author:
W. Brent Edwards
University of Illinois at Chicago
Department of Kinesiology and Nutrition
1919 W. Taylor Street
650 AHSB, M/C 517
Chicago, IL 60612
Phone: 312-996-1582
E-mail: edwardsb@uic.edu

ABSTRACT

To better understand the mechanisms underlying distal radius fracture we have developed finite element models to predict radius bone strain and fracture strength under loading conditions simulating a fall. This study compares experimental surface strains and fracture loads of the distal radius with specimen-specific finite element models to validate our model-generating algorithm. Five cadaveric forearms were instrumented with strain gage rosettes, loaded non-destructively to 300 N, and subsequently loaded until failure. Finite element models were created from computed tomography data; three separate density-elasticity relationships were examined. Fracture strength was predicted for three specimens that failed at the distal radius using six different failure theories. The density-elasticity relationship providing the strongest agreement between measured and predicted strains had a correlation of r=0.90 and a root mean squared error 13% of the highest measured strain. Mean absolute percent error (11.6%) between measured and predicted fracture loads was minimized with Coulomb-Mohr failure theory and a tensile-compressive strength ratio of 0.5. These results suggest that our modeling method is a suitable candidate for the *in vivo* assessment of distal radius bone strain and fracture strength under fall type loading configurations.

Keywords: Finite element model; Density-elasticity relationship; Failure criteria; Experimental validation; Falls

INTRODUCTION

Distal radius fractures are the most common upper extremity fractures in adults 65 years and older [1]. Nearly 80% of distal radius fractures result from a fall [2]. Because many of these falls occur from standing height or lower, fractures of the distal radius are considered low-energy fractures and are associated with age-related declines in bone quality. Distal radius fractures are a source of considerable morbidity; approximately 40% of all dollars spent on physical therapy following osteoporotic fractures go to treat the distal forearm, 50% of patients are dissatisfied with their functional outcome six months post-fracture, and more than one third experience pain or weakness [3].

The propensity for skeletal fracture to occur as a result of a fall is dependent on the loading intensity during impact (i.e., stress and strain within the bone itself). Previous research has focused on preventive strategies, such as surface compliance [4] and fall arrest manipulations [5], to reduce peak bone loading. These studies have used the external reaction force as a surrogate measure of bone loading because the direct measurement of bone strain *in vivo* requires invasive surgical procedures [6]. Unfortunately, the relationship between external force and internal bone loading is often complex and nonintuitive. This is because external forces generate location-specific triaxial stress-strain states that are dependent on bone size, shape, and material properties. Thus, the ability to quantify radius bone strain non-invasively, and ultimately define fracture strength, would greatly aid in the development and evaluation of preventive measures to minimize the occurrence of distal radius fracture.

Subject-specific finite element models have been an effective tool for both bone strain and fracture strength assessment. The accuracy of these models is heavily dependent on the chosen constitutive equation that relates stress to strain [7, 8], and the chosen failure criterion that defines fracture threshold [9]. The purpose of this study was to compare experimental surface strains and fracture loads of the distal radius with specimen-specific finite element models for the purpose of validating our model-generating algorithm. Our immediate use for the model is to gain a better understanding of the mechanisms underlying distal radius fracture. For this reason, the model was validated under loading conditions simulating a fall.

METHODS

Specimens

Five female cadaveric right forearms with hand intact (mean age 78 yrs, range 59-93 yrs) were obtained through anatomical gift. Specimens were freshly-frozen and stored at -20 °C, but thawed to room temperature for: 1) computed tomography (CT) data acquisition 2) specimen dissection and potting and 3) strain gage application and mechanical testing. In these instances, a saline solution spray was used periodically to keep the specimens moist. The distal most 12 cm of the forearms were imaged with a clinical CT scanner (BrightSpeed; GE Medical Systems, Milwaukee, WI, 120 kV, 180 mA, voxel size: 234 x 234 x 625 μm). Images were reconstructed with GE's high spatial frequency (bone) algorithm. A subsequent identical scanning session of a calibration phantom (QRM, Moehrendorf, Germany) with calcium hydroxyapatite equivalent concentrations of 0, 400, and 800 mg/cm^3 was used to establish the following linear relationship between CT Hounsfield units (Hu) and calcium hydroxyapatite equivalent density (ρ_{ha}) in g/cm^3:

$$\rho_{ha} = 0.0069 + 0.0007 * \mathrm{Hu} \quad (r^2 = 0.9993).$$

Experimentation

All soft tissue proximal to the wrist joint capsule was removed and radial/ulnar osteotomy was performed 14 cm proximal to Lister's Tubercle. The proximal most 8 cm of the forearms were embedded in polymethylmethacrylate (PMMA), leaving 6 cm exposed below

Lister's Tubercle (Figure 1). Six rectangular strain gage rosettes (TS1N-K120M-PK06-LE, Micro-Flextronics Ltd, Coleraine, N. Ireland) were adhered circumferentially to the periosteal surface of the radius. The active gage length for each individual grid within the rosette was 1.5 mm, which corresponded to an overall gage length of 4.2 mm in a stacked rosette configuration. Three rosettes were mounted distally, immediately proximal to Lister's Tubercle, and three were mounted 3 cm proximal to the distal gage locations (Figure 1). These two locations were chosen to elicit a large range in periosteal surface strains – whereas the distal location was comprised primarily of trabecular bone, the proximal location was comprised primarily of cortical bone. Prior to strain gage attachment the periosteum was removed, the surface was cleaned with isopropyl alcohol, sanded, and recleaned with isopropyl alcohol. Gages were adhered with cyanoacrylate glue and covered with a polyurethane coating.

For strain assessment, specimens were loaded in compression using a uniaxial-driven materials testing machine (MiniBionix 858, MTS Systems, Eden Prairie, MN). Force was applied to the palm of the hand with a custom made fixture mounted to the load actuator (Figure 2). The fixture consisted of a flat aluminum plate with an angular adjustment to mimic ground contact during a fall onto an outstretched hand. The aluminum plate was angled 60° from vertical such that the wrist was extended 60° to simulate falling conditions [10]. The amount of wrist extension was confirmed by a goniometer and an additional aluminum plate was brought into contact with the dorsal surface of the hand to prevent further extension. The bottom surface of the PMMA was placed on a smooth, flat, unconstrained aluminum surface mounted to the MTS load cell. The PMMA was sanded and coated with lubricant to reduce frictional shear forces during testing [11]. The actuator was driven at a fixed displacement rate of 0.1 mm/s until a load of 300 N was reached. Force and displacement data were collected concurrently at 100 Hz, and an additional six synchronized analog channels were available for strain information. Therefore, only data from two rosettes could be collected during each test. Fifteen total tests were performed allowing for five repeat trials to be collected for each gage. Load repetitions were separated by approximately two minutes. Following strain assessment, specimens were loaded in an identical fashion until failure. The fracture load was identified by a rapid decrease in the slope of the force/displacement curve. Strain gage locations within the CT imaging coordinate system were determined following mechanical testing, by overlaying dissected cross sections of the specimens with their respective CT images.

Modeling

Stereolithographic models of the radius, scaphoid, and lunate based on segmented CT data from Mimics (Materialise, Leuven, Belgium) were imported into IA-FEMesh (University of Iowa, Iowa City, IA) for finite element model creation (Figure 3). IA-FEMesh allows the user to define a series of blocks around the surface of interest. Each block is composed of a mesh seeding with a user-specified refinement that is projected onto the surface, laying the foundation for the finite element geometry [12]. The models consisted of 18,231 ± 2,402 8-node hexahedral elements with 21,406 ± 2,600 degrees of freedom depending on specimen size. A nominal element size of 1 mm^3 was chosen in accordance with a preliminary mesh convergence analysis. The scaphoid and lunate were modeled as non-deformable rigid bodies. Articular cartilage was included in the model by extruding elements of the radial-carpal bone articular surface 1 mm [13] in a local-normal direction (producing a tissue thickness “just touching” the carpal bones). The cartilage was modeled as a neo-Hookean hyperelastic material with a modulus of 10 MPa [14]; near-incompressibility was assumed [15], thus Poisson’s ratio was set to 0.49. For the radius, internal elements were assigned the median ρ_{ha} of the comprising voxels; surface elements were assigned the maximum ρ_{ha} to avoid partial volume effects. Three previously established density-elasticity relationships (Eqs. i – iii) were investigated that allowed for inhomogeneous linearly-isotropic material properties to be assigned to the finite element models (Figure 3):

(i) $E = 10500\rho_{ash}^{2.29}$ [16],

(ii) $E = 6950\rho_{app}^{1.49}$ [17],

(iii) $E = 2875\rho_{app}^{3}$ [18],

where E is expressed in MPa, and ρ_{app} (apparent density) and ρ_{ash} (ash density) are expressed in g/cm^3. For Eq. (i), calcium hydroxyapatite equivalent density was converted to ρ_{ash} using:

$$\rho_{ash} = 0.0698 + 0.839\rho_{ha} \text{ [19].}$$

For Eqs. (ii) and (iii), ρ_{ash} was divided by 0.6 to obtain ρ_{app} [8]. Moduli lower than 0.01 MPa were assigned a new value of 0.01 MPa [20]. We determined that sufficient model accuracy (% change in principal strains less than 1%) could be obtained by binning moduli in increments corresponding to 20 Hu, or ρ_{ha} = 0.014 g/cm^3. However, moduli were binned in increments corresponding to 10 Hu, or ρ_{ha} = 0.007 g/cm^3, because the increased computational time was negligible. This resulted in 239 ± 13 bins ranging from 0.01 to 21,547 ± 2,728 MPa for Eq. (i), 23,714 ± 1,997 MPa for Eq. (ii), and 34,218 ± 5,565 MPa for Eq. (iii), depending on ρ_{ha} range. Each bin was assigned a Poisson's ratio of 0.4 [11, 21].

Finite element analyses were performed using FEBio software (Musculoskeletal Research Laboratories, Salt Lake City, UT). The proximal end of the radius was fully constrained at the location of potting. To simulate the boundary conditions imparted by 60° wrist extension, the scaphoid and lunate were rotated about the flexion-extension axis 50° and 35°, respectively. These rotations were based on average values from *in vivo* and *in vitro* examinations of carpal bone kinematics as a function of wrist angle [22, 23]. Contact was modeled between the surfaces of the radius and scaphoid, and the radius and lunate. We assumed that during load application, the radial-carpal ligaments and wrist joint capsule kept the carpal bones seated within the articular cartilage. Therefore, a "tied" interface contact model was utilized in which the carpal bones were not free to slide once initial contact was made. The contact constraints were enforced using the augmented Lagrangian method [24]. A ramped quasi-static load of 300 N was applied to the centroids of the scaphoid (180 N) and lunate (120 N) based on the assumption that the scaphoid bears 60% of the load transmitted through the wrist [25, 26]. The line of action of the resultant force vector was determined for each specimen using an unsymmetrical beam theory analysis based on proximal strain gage and CT information (Figure 4; See Appendix for specific details).

Bone failure was simulated with the finite element method by applying a ramped load up to 3000 N in increments of 120 N. Six different stress- and strain-based failure criteria were evaluated based on previous successful predictions of distal radius fracture [27] and femoral fracture load [9]. These criteria, which are summarized in Table 1, assume that element failure will occur when the factor of safety is less than or equal to 1. The Coulomb-Mohr (CM), Hoffman (H_σ), Hoffman Strain Analog (H_ε), and Maximum Principal Strain (ε_{max}) theories allow for different tensile (σ_{yt}, ε_{yt}) and compressive (σ_{yc}, ε_{yc}) failure strengths. Assuming, $\sigma_{yt}=k\ \sigma_{yc}$ and $\varepsilon_{yt}=k\ \varepsilon_{yc}$, we examined four different values of k to investigate a range of material behaviors: 1, 0.75, 0.5, and 0.25. In general, a material's behavior becomes more brittle as the tensile-compressive strength ratio, k, approaches zero [28]. Cortical bone was assigned an ε_{yc} of 0.0154 [29] and cancellous bone an ε_{yc} of 0.011 [30]; σ_{yc} was determined by multiplying ε_{yc} by the respective element's E. For both cortical and cancellous bone, γ_y was assigned a value 0.0146

[31]. Failure was determined for each element at each load increment. Bone fracture (i.e., crack propagation) was assumed to occur when a cluster of contiguous failed elements exceeded a predefined volume. A failed volume of approximately 150 mm^3 has been proposed for micro-finite element models of the distal radius [27], while 405 mm^3 has been proposed for continuum models of the proximal femur [11]. Thus, we examined a range of failed volumes from 150 to 450 mm^3, in increments of 100 mm^3.

Data Analysis

Experimental strain readings from each rosette were used to calculate maximum and minimum principal strains at the instant the target load of 300 N was reached. The between-trial reliability of principal strains at 300 N was examined using interclass correlations (ICC) and variability was assessed using standard error of measurement (SEM), where SEM = standard deviation*$(1\text{-ICC})^{½}$ [32]. Model predicted strains for nodes corresponding to each rosette location were transformed into a local coordinate system with a unit normal to the model exterior surface. Maximum and minimum principal strains in the surface plane were calculated and nodal values were averaged at each rosette location. Model predicted and experimentally measured principal strains at 300 N were compared using Pearson's r correlation, linear regression, root mean squared error (RMSE), and maximum error (Max err). The criterion alpha level was set to 0.05 for ICC, Pearson's r, and linear regression analyses. Scatter was assessed using Bland-Altman plots. These illustrate the difference between predicted and measured strains, expressed as a percentage of the mean, versus the mean of the predicted and measured strains. The density-elasticity relationship resulting in the highest correlation and least amount of error was used for failure simulations. Discrepancies between modeled and experimental fracture loads were expressed as a percent error, and the correspondence in fracture location was examined qualitatively.

RESULTS

Experimentation

Experimentally measured principal strains were highly reliable (gage dehiscence occurred for the distal strain gages of a single specimen during mechanical testing, so these data were not included). For example, the ICC for maximum principal strains at 300 N measured across 5 trials was 0.997 ($p<0.001$); ICC was 0.994 ($p<0.001$) for minimum principal strains. The SEM was 10 $\mu\varepsilon$ for maximum principal strains and 18 $\mu\varepsilon$ for minimum principal strains. These SEM values corresponded to approximately 1.6% and 1.8% of the largest measured maximum (640 $\mu\varepsilon$) and minimum (-977 $\mu\varepsilon$) principal strain, respectively.

Of the five specimens loaded until failure, three fractured at the distal radius, one fractured at the scaphoid, and one wrist dislocated. Interestingly, the line of action of the resultant force vector fell outside the bone cross section for the dislocated specimen, indicating poor alignment of the specimen within the testing fixture (Figure 4). Only the three specimens with distal radius fracture were used for failure analysis. Distal radius fracture occurred at loading magnitudes of 813, 971, and 1,214 N.

Comparison between predicted and measured strains

The finite element predicted strains varied as a function of Eqs. (i-iii) (Figure 5). Correlation coefficients for experimentally measured strains versus predicted strains ranged from $r=0.90$ ($p<0.001$) for Eq (i) to $r=0.86$ ($p<0.001$) for Eq (ii) (Table 2). For Eqs. (i) and (iii) regression slopes were not different from unity ($p\geq0.270$) and intercepts were not different from zero ($p\geq0.178$). Despite having a relatively high correlation coefficient and an intercept that was not different from zero ($p=0.056$), the regression slope for Eq. (ii) was different from unity ($p<0.001$). The RMSE among density-elasticity Eqs. ranged from 13% to 14% of the highest measured strain. Max error was smallest for Eq. (i) and largest for Eq. (ii).

Bland-Altman plots illustrated a randomly distributed scatter across strain magnitudes for Eqs. (i) and (iii) (Figure 5). In contrast, Eq. (ii) illustrated systematic scatter in which strains were under-predicted at high strain magnitudes and over-predicted at low strain magnitudes. Overall, predicted strains using the Eq. (i) were most closely matched to measured strains in terms of regression coefficients, error, and scatter. Therefore, the finite element models created using Eq. (i) were used for failure analyses.

Comparison between predicted and measured fracture loads

The predicted fracture loads varied among failure theories, tensile-compressive strength ratio *k,* and contiguous volume assumptions. For a given failure theory and volume, changing *k* from 0.25 to 0.5, from 0.5 to 0.75, and from 0.75 to 1 increased fracture loads an average of 26%, 9%, and 4%, respectively.*,* For a given failure theory and *k*, changing volume from 150 to 250 mm^3, from 250 to 350 mm^3, and from 350 to 450 mm^3 increased fracture loads an average of 7%, 5%, and 4%, respectively. For a contiguous volume of 150 mm^3, mean absolute percent error was minimized with H_σ theory and $k=0.5$ (Figure 6). For contiguous volumes of 250, 350, and 450 mm^3, mean absolute percent error was minimized with CM theory and $k=0.5$. In all of these instances, mean absolute percent error varied from 11.6% (range 2.2-25.4% for 350 mm^3) to 12.9% (range 3.90-18.45% for 150 mm^3).

The centroids of failed contiguous volumes were located within the distal radius cancellous region for all failure theories. Crack propagation was not explicitly simulated and as such, failed elements (failure criterion value ≥ 1) were not observed at the external surface of the models. However, the CM failure contours (k=0.5) illustrated higher values at locations where experimental fracture manifested at the surface (Figure 7).

DISCUSSION

Non-invasive methods to quantify bone strain and fracture strength on a subject-specific basis are needed so that preventive measures to reduce the incidence of distal radius fracture can be evaluated. The purpose of this study was to compare experimental surface strains and fracture loads at the distal radius with specimen-specific finite element models to validate our model generating algorithm. Of the three density-elasticity relationships investigated, the models developed using Eq. (i) [16] predicted principal strains that most closely matched the experimentally measured strains. Average percent error between experimentally measured and model predicted fracture loads was minimized with the use of CM failure theory, a tensile-compressive strength ratio k=0.5, and a contiguous volume assumption of 350 mm^3. In addition, surface elements illustrating the largest magnitudes of CM failure qualitatively agreed with the locations where experimental fracture was observed at the surface.

Very few studies have investigated the influence of density-elasticity relationships on the accuracy of specimen-specific finite element predicted strains [7, 8, 33]. Schileo *et al.* [8] compared three density-elasticity relationships for the human femur under several loading scenarios and concluded that the relationship described by Morgan *et al.* [17], Eq. (ii) in the present study, produced the closest agreement between numerical and experimental results. Austman *et al.* [7] compared six density-elasticity relationships for the human ulna under a simplified cantilever bending scenario and observed the most accurate results using the Carter and Hayes relationship [18], corresponding to Eq. (iii) here, as well as a pooled bone site relationship described by Morgan *et al*. [17]. The discrepancy in density-elasticity relationship accuracy between the current and aforementioned studies is not surprising. Density-elasticity relationships depend on variables such as anatomical site [17] and strain rate [18]. Eq. (ii), which provided the poorest agreement between experimental and predicted surface strains in the present study, was developed for femoral trabecular bone. Similar to Austman et al. [7], we found reasonable agreement with Eq. (iii), which is logical given the anatomic similarity of the radius and ulna. Unfortunately, we are unaware of a density-elasticity relationship specific to the distal radius. We hesitate to implicate strain rate as a discriminating factor in the present study because all three density-elasticity relationships investigated were determined using strain rates of 0.01 to 1 s^{-1} [16-18]. Our strain rates were substantially lower than this with maximum measured values of 2.5×10^{-4} to 4.5×10^{-4} s^{-1}.

Here, we observed a best-fit correlation of 0.90 between experimental and predicted strains using Eq. (i). Similar *in vitro* validation studies have reported various levels of accuracy ranging from r=0.679 to 0.955 [8, 34-38]. Several factors can explain this relatively large range in model accuracy including: the number of specimens used, constitutive law applied, loading scenario(s) investigated, as well as the incorporated model meshing technique (voxel vs. geometry based). These studies focused on the femur, pelvis, and scapula. In all cases but one [36], complex bone articulations were not incorporated into *in vitro* testing and modeling. This approach is sufficient for bones like the femur, for which the boundary conditions in a fall-type load configuration are relatively straightforward (e.g. side impact to the greater trochanter). For the wrist however, load is transferred to the distal radius through its articulating carpal bones.

Finite element models developed to examine the mechanisms underlying distal radius fracture should be validated with the wrist joint fully intact, allowing the model's behavior under physiological loading conditions to be investigated. It is important to note that our accuracy in predicted strain is dependent on how well our finite element model represents both the structural characteristics of and boundary conditions applied to the radius. The boundary conditions that were applied to the scaphoid and lunate were estimated based on measured surface strains and radius geometry. Both of these quantities are direct and repeatable measures derived from the bone itself. In contrast, the finite element model involves some assumptions about how density relates to modulus of elasticity, and how to best simulate element failure. Our interpretation is that these last two assumptions are the true subject of the finite element model validation. Although we adopted a method to approximate the line of action of the resulting force vector based on unsymmetrical beam theory, there is still some uncertainty in simulating this "physiological" contact scenario including: the exact load share distribution between the scaphoid and lunate, the exact carpal bone translations/rotations that occur relative to the radius with wrist extension, and the possibility of shear forces at the lubricated PMMA/aluminum interface. Changes in these parameters can influence load transition through the radius [39] and thus periosteal surface strain, and may have contributed to our observed error.

The volume of failed contiguous elements chosen to represent bone fracture in this study was a topic of uncertainty. This approach, which has been used by others to predict the fracture strength of the distal radius [27, 40] and proximal femur [11, 20], assumes that a given amount of tissue must fail in order for a crack to propagate. This approach also reduces the potential error caused by CT scanning and finite element modeling artifacts that may underestimate the failure strength of individual elements. Although, changing this volume influenced the predicted fracture load, the mean absolute percent errors were not substantially altered by volume assumption (See Figure 6). This is because the most accurate volume for fracture strength prediction varied amongst specimens. This specific response may be related to differences in the age of the specimens tested to failure (59, 71, and 93 yrs). The bone of younger adults can undergo more plastic deformation before failure [41], which would require an increased contiguous volume assumption to replicate in our linear elastic models. Further study with an increased sample size and a thorough statistical analysis would be necessary to verify this assumption.

Here we observed a fracture strength prediction accuracy of 11.6 to 12.9%, depending on the chosen contiguous volume. This is comparable to the 13% accuracy reported for microCT finite element models of the distal radius [27]. Our most accurate predictions were obtained using CM and H_σ theories with k=0.5. Investigations of bovine trabecular bone have reported tensile-compressive strength ratios ranging from 0.3 to 0.7 [42, 43]. Both CM and H_σ theories are stress-based criteria intended to be applicable across a range of material types (i.e., ability to account for different tensile and compressive strengths). In their simplest form where k=1, CM and H_σ theories are equivalent to Tresca (max shear stress) and von Mises (max distortion energy) criteria, respectively. These findings suggest that shear or distortion modes of failure play an important role in bone fracture, at least at the continuum level. At the microstuctural level, bone fracture is indeed strain controlled [44]. Thus from a theoretical standpoint the appropriate failure criterion should be strain-based as well. Unfortunately, our continuum and linearly isotropic assumptions do not allow us to properly model the microstructural properties of bone. For present purposes it is more important to determine a robust failure theory that phenomenologically describes fracture load and location given the various simplifications and limitations of the modeling procedure.

This study is limited by the relatively small sample size of five specimens for strain assessment and three specimens for failure analysis. However, most specimen specific finite element model validation studies have relied on sample sizes of three or less [34-38, 45, 46], with only a few having reported sample sizes greater than this [8, 11]. Here, we dealt with partial volume effects by assigning surface elements the maximum density of the comprising voxels, which could be considered a less refined method than other published techniques [47], and may have contributed to the observed scatter between measured and predicted strains. However, given the homogeneity of cortical bone, variation in Hu within elements at the bone surface would largely be explained by partial volume artifacts, providing rationale for the assignment of maximum density.

For this initial validation, a slow rate of loading (0.1 mm/s) was used for fracture analysis corresponding to approximately 10-20 N/s. Actual loading rates during a fall can approach 90 to 180 kN/s [48]. Our future work will focus on validating similar models able to predict bone strain and fracture load at rates of loading consistent with a fall. Presumably, this would require us to incorporate strain-rate dependent behavior into our models, which could be done for Young's modulus by including a second power-term in the density-elasticity relationship [18]. Additionally, bone elicits a ductile-to-brittle transition with increases in strain rate, which influences post-yield behavior [49]. This would likely require smaller contiguous volume assumptions [46] and different ultimate failure strengths. Alternatively, an elastic-plastic material model could be incorporated with strain-rate dependent post-yield behavior. Such a material model would also likely improve our overall prediction accuracy [50].Unfortunately we were unable to compare experimental and predicted fracture location in a quantitative manner. This stems from our inability to identify the location of fracture onset during experimentation. Future studies could incorporate high-speed video to approximate the location of fracture onset [46], provided that crack nucleation occurred at the periosteal surface.

In summary, the present study has shown that our model generating algorithm provides realistic measures of radius bone strain and fracture strength under a physiological loading scenario simulating a fall. Given our model's level of accuracy for strain (r=0.90, RMSE=13% of the highest measured strain) and fracture prediction (mean absolute percent error of 11.6%), we consider it a suitable candidate for *in vivo* examinations of preventive strategies to minimize the occurrence of distal radius fracture.

ACKNOWLEDGEMENTS

Partial funding for this study was provided by the Department of Kinesiology and Nutrition at the University of Illinois at Chicago.

CONFLICT OF INTEREST

The authors have no conflict of interest

APPENDIX A

The axial force, P, and bending moments, Mx and My, acting at the cross section corresponding to the proximal gage locations were resolved using unsymmetrical beam theory as described by Rybicki et al., [51]. Assuming the origin of the reference system is at the cross section centoid, the axial strain ε_{zz} at any point (x, y) can be determined as:

$$\varepsilon_{zz} = \varepsilon_0 + \kappa_y x + \kappa_x y$$

where ε_0 is the strain created by the axial force, and κ_y and κ_x are the radii of curvature about the x and y-axis, respectivity. Using the measured strain from the axial gage at each of the three rosette locations the unknown parameters ε_0, κ_y, and κ_x can be determined. The axial force, P, and bending moments, Mx and My, acting at the cross section are then:

$$P = E(A\varepsilon_0)$$

$$M_x = E(\kappa_x I_{xx} + \kappa_y I_{xy})$$

$$-M_y = E(\kappa_x I_{xy} + \kappa_y I_{yy})$$

where E is the elastic modulus, A is the cross sectional area, and I_{xx}, I_{yy}, and I_{xy} are the cross sectional moments of inertia defined as:

$$A = \sum_{i=1}^{n} dA_i$$

$$I_{xx} = \sum_{i=1}^{n} y_i^2 \cdot dA_i$$

$$I_{yy} = \sum_{i=1}^{n} x_i^2 \cdot dA_i$$

$$I_{xy} = \sum_{i=1}^{n} (xy)_i \cdot dA_i$$

were n is the number of bone pixels and dA_i is the i^{th} bone pixel area. The line of action of the applied force was then calculated by assuming that it was directed from the scaphoid and lunate centroids through location (x_{act}, y_{act}), using the following formulae:

$$x_{act} = \frac{My}{P} \text{ and } y_{act} = \frac{-Mx}{P}.$$

It can be seen that the calculation of x_{act} and y_{act} is independent of the chosen E.

REFERENCES

[1] Vogt MT, Cauley JA, Tomaino MM, Stone K, William JR, Herndon JH. Distal Radius Fractures in Older Women: A 10-Year Follow-Up Study of Descriptive Characteristics and Risk Factors. the Study of Osteoporotic Fractures. Journal of the American Geriatrics Society 2002; **50**(1): 97-103.

[2] Oskam J, Kingma J, Klasen HJ. Fracture of the Distal Forearm: Epidemiological Developments in the Period 1971-1995. Injury 1998; **29**(5): 353-355.

[3] Melton LJ. Adverse Outcomes of Osteoporotic Fractures in the General Population. Journal of Bone and Mineral Research 2003; **18**(6): 1139-1141.

[4] Robinovitch SN, Chiu J. Surface Stiffness Affects Impact Force during a Fall on the Outstretched Hand. Journal of Orthopaedic Research 1998; **16**(3): 309-313.

[5] Kim KJ, Ashton-Miller JA. Biomechanics of Fall Arrest using the Upper Extremity: Age Differences. Clinical Biomechanics 2003; **18**(4): 311-318.

[6] Foldhazy Z, Arndt A, Milgrom C, Finestone A, Ekenman I. Exercise-Induced Strain and Strain Rate in the Distal Radius. The Journal of Bone and Joint Surgery 2005; **87**(2): 261-266.

[7] Austman RL, Milner JS, Holdsworth DW, Dunning CE. The Effect of the Density-Modulus Relationship Selected to Apply Material Properties in a Finite Element Model of Long Bone. Journal of Biomechanics 2008; **41**(15): 3171-3176.

[8] Schileo E, Taddei F, Malandrino A, Cristofolini L., Viceconti M. Subject-Specific Finite Element Models can Accurately Predict Strain Levels in Long Bones. Journal of Biomechanics 2007; **40**(13): 2982-2989.

[9] Keyak JH, Rossi SA. Prediction of Femoral Fracture Load using Finite Element Models: An Examination of Stress- and Strain-Based Failure Theories. Journal of Biomechanics 2000; **33**(2): 209-214.

[10] Troy KL, Grabiner MD. Asymmetrical Ground Impact of the Hands After a Trip-Induced Fall: Experimental Kinematics and Kinetics. Clinical Biomechanics 2007; **22**(10): 1088-1095.

[11] Keyak JH, Rossi SA, Jones KA, Skinner HB. Prediction of Femoral Fracture Load using Automated Finite Element Modeling. Journal of Biomechanics 1998; 31(2): 125-133.

[12] Grosland NM, Shivanna KH, Magnotta VA, Kellemeyn NA, DeVries NA, Tadepalli SC, Lisle C. IA-FEMesh: An Open-Source, Interactive, Multiblock Approach to Anatomic Finite Element Model Development. Computer Methods and Programs in Biomedicine 2009; **94**(1): 96-107.

[13] Pillai RR, Thoomukuntla B, Ateshian GA, Fischer KJ. MRI-Based Modeling for Evaluation of in Vivo Contact Mechanics in the Human Wrist during Active Light Grasp. Journal of Biomechanics 2007; **40**(12): 2781-2787.

[14] Anderson DD, Deshpande BR, Daniel TE, Baratz ME. A Three-Dimensional Finite Element Model of the Radiocarpal Joint: Distal Radius Fracture Step-Off and Stress Transfer. The Iowa Orthopaedic Journal 2005; **25**: 108-117.

[15] Armstrong CG, Lai WM, Mow VC. An Analysis of the Unconfined Compression of Articular Cartilage. Journal of Biomechanical Engineering 1984; **106**(2): 165-173.

[16] Keller TS. Predicting the Compressive Mechanical Behavior of Bone. Journal of Biomechanics 1994; **27**(9): 1159-1168.

[17] Morgan EF, Bayraktar HH, Keaveny TM. Trabecular Bone Modulus-Density Relationships Depend on Anatomic Site. Journal of Biomechanics 2003; **36**(7): 897-904.

[18] Carter DR, Hayes WC. The Compressive Behavior of Bone as a Two-Phase Porous Structure. The Journal of Bone and Joint Surgery 1977; **59**(7): 954-962.

[19] Kaneko TS, Bell JS, Pejcic MR, Tehranzaden J, Keyak JH. Mechanical Properties Density and Quantitative CT Scan Data of Trabecular Bone with and without Metastases. Journal of Biomechanics 2004; **37**(4): 523-530.

[20] Keyak JH, Rossi SA, Jones KA, Les CM, Skinner HB. Prediction of Fracture Location in the Proximal Femur using Finite Element Models. Medical Engineering & Physics 2001; **23**(9): 657-664.

[21] Reilly DT, Burstein AH. The Elastic and Ultimate Properties of Compact Bone Tissue. Journal of Biomechanics 1975; **8**(6): 393-405.

[22] Moojen TM, Snel JG, Ritt MJ, Kauer JM, Verema HW, Bos KE. Three-Dimensional Carpal Kinematics in Vivo. Clinical Biomechanics 2002; **17**(7): 506-514.

[23] Kobayashi M, Berger RA, Nagy L, Linscheid RL, Uchiyama S, Ritt M, An KN. Normal Kinematics of Carpal Bones: A Three-Dimensional Analysis of Carpal Bone Motion Relative to the Radius. Journal of Biomechanics 1997; **30**(8): 787-793.

[24] Mass S, Rawlins D, Weiss J, Ateshian G FEBio Theory Manual Version 1.2 URL: http://mrl.sci.utah.edu/software/febio

[25] Majima M, Horii E, Matsuki H, Hirata H, Genda E. Load Transmission through the Wrist in the Extended Position. The Journal of Hand Surgery 2008; 33(2): 182-188.

[26] Schuind F, Cooney WP, Linscheid RL, An KN, Chao EY. Force and Pressure Transmission through the Normal Wrist. A Theoretical Two-Dimensional Study in the Posteroanterior Plane. Journal of Biomechanics 1995; **28**(5): 587-601.

[27] Pistoia W, van Rietbergen B, Lochmuller EM, Lill CA, Eckstein F, Ruegsegger P. Estimation of Distal Radius Failure Load with Micro-Finite Element Analysis Models Based on Three-Dimensional Peripheral Quantitative Computed Tomography Images. Bone 2002; **30**(6): 842-848.

[28] Christensen, RM. A Two-Property Yield, Failure (Fracture) Criterion for Homogeneous, Isotropic Materials. Journal of Engineering Materials and Technology 2004; **126**: 45-52.

[29] Steinhauser E, Diehl P, Hadaller M Schauwecker J, Busch R, Gradinger R, Mittelmeier W. Biomechanical Investigation of the Effect of High Hydrostatic Pressure Treatment on the Mechanical Properties of Human Bone. Journal of Biomedical Materials Research. Part B Applied Biomaterials 2006; **76**(1): 130-135.

[30] Rohl L, Larsen E, Linde F, Odgaard A. Tensile and Compressive Properties of Cancellous Bone. Journal of Biomechanics 1991; 24(12): 1143-1149.

[31] Ford CM, Keaveny TM. The Dependence of Shear Failure Properties of Trabecular Bone on Apparent Density and Trabecular Orientation. Journal of Biomechanics 1996; **29**(10): 1309-1317.

[32] Harvill LM. Standard Error of Measurement. Educational Measurement: Issues and Practice 1991; **10**: 33-41.

[33] Barker DS, Netherway DJ, Krishnan J, Hearn TC. Validation of a Finite Element Model of the Human Metacarpal. Medical Engineering & Physics 2005; **27**(2): 103-113.

[34] Ota T, Yamamoto I, Morita R. Fracture Simulation of the Femoral Bone using the Finite-Element Method: How a Fracture Initiates and Proceeds. Journal of Bone and Mineral Metabolism 1999; **17**(2): 108-112.

[35] Gupta S, van der Helm FC, Sterk JC, van Keulen F, Kaptien BL. Development and Experimental Validation of a Three-Dimensional Finite Element Model of the Human Scapula. Proceedings of the Institution of Mechanical Engineers. Part H Journal of Engineering in Medicine 2004; **218**(2): 127-142.

[36] Anderson AE, Peters CL, Tuttle BD, Weiss JA. Subject-Specific Finite Element Model of the Pelvis: Development Validation and Sensitivity Studies. Journal of Biomechanical Engineering 2005; **127**(3): 364-373.

[37] Keyak JH, Fourkas MG, Meagher JM, Skinner HB. Validation of an Automated Method of Three-Dimensional Finite Element Modelling of Bone. Journal of Biomedical Engineering 1993; **15**(6): 505-509.

[38] Taddei F, Cristofolini L, Martelli S, Gill HS, Viceconti M. Subject-Specific Finite Element Models of Long Bones: An in Vitro Evaluation of the overall Accuracy. Journal of Biomechanics 2006; **39**(13): 2457-2467.

[39] Ulrich D, van Rietbergen B, Laib A, Ruegsegger P. Load Transfer Analysis of the Distal Radius from in-Vivo High-Resolution CT-Imaging. Journal of Biomechanics 1999; 32(8): 821-828.

[40] Troy KL, Grabiner MD. Off-Axis Loads Cause Failure of the Distal Radius at Lower Magnitudes than Axial Loads: A Finite Element Analysis. Journal of Biomechanics 2007; **40**(8): 1670-1675.

[41] Bernstein AH, Reilly D T, Martens M. Aging of Bone Tissue: Mechanical Properties. Journal of Bone and Joint Surgery 1976; **58**: 82-86.

[42] Keaveny TM, Wachtel EF, Ford C M, Hayes WC. Differences between the Tensile and Compressive Strengths of Bovine Tibial Trabecular Bone Depend on Modulus. Journal of Biomechanics 1994; **27**(9): 1137-1146.

[43] Stone JL, Beaupre GS, Hayes W C. Multiaxial Strength Characteristics of Trabecular Bone. Journal of Biomechanics 1983; **16**(9): 743-752.

[44] Nalla RK, Kinney JH, Ritchie RO. Mechanistic Fracture Criteria for the Failure of Human Cortical Bone. Nature Materials 2003; **2**(3): 164-168.

[45] Gray HA, Taddei F, Zavatsky AB, Cristofolini L, Gill HS. Experimental Validation of a Finite Element Model of a Human Cadaveric Tibia. Journal of Biomechanical Engineering 2008; **130**(3): 031016-1-9.

[46] Schileo E, Taddei F, Cristofolini L, Viceconti M. Subject-Specific Finite Element Models Implementing a Maximum Principal Strain Criterion are Able to Estimate Failure Risk and Fracture Location on Human Femurs Tested in Vitro. Journal of Biomechanics 2008; **41**(2): 356-367.

[47] Helgason B, Taddei F, Palsson H Schileo E, Cristofolini L, Viceconti M, Brynjolfsson S. A Modified Method for Assigning Material Properties to FE Models of Bones. Medical Engineering & Physics 2008; **30**(4): 444-453.

[48] DeGoede KM, Ashton-Miller JA, Schultz AB. Fall-Related Upper Body Injuries in the Older Adult: A Review of the Biomechanical Issues. Journal of Biomechanics 2003; **36**(7): 1043-1053.

[49] Hansen U, Zioupos P, Simpson R, Currey JD, Hynd D. The Effect of Strain Rate on the Mechanical Properties of Human Cortical Bone. Journal of Biomechanical Engineering 2008; **130**(1): 011011.

[50] Keyak JH. Improved Prediction of Proximal Femoral Fracture Load using Nonlinear Finite Element Models. Medical Engineering & Physics 2001; **23**(3): 165-173.

[51] Rybicki EF, Mills EJ. In Vivo and Analytical Studies of Forces and Moments in Equine Long Bones. Journal of Biomechanics 1977; **10**(11/12): 701-705.

TABLES

Table 1. The six failure criterion investigated with their respective equations.

Criterion	Equation
CM (Coulomb-Mohr)	$(\sigma_1/\sigma_{yt})-(\sigma_3/\sigma_{yc}) \geq 1$
H_σ (Hoffman)	$(1/2\sigma_{yt}\sigma_{yc})[(\sigma_1-\sigma_2)^2+(\sigma_1-\sigma_3)^2(\sigma_2-\sigma_3)^2]+\ldots$ $[(1/\sigma_{yt})-(1/\sigma_{yc})](\sigma_1+\sigma_2+\sigma_3) \geq 1$
H_ε (Hoffman Strain Analog)	$(1/2\varepsilon_{yt}\varepsilon_{yc})[(\varepsilon_1-\varepsilon_2)^2+(\varepsilon_1-\varepsilon_3)^2(\varepsilon_2-\varepsilon_3)^2]+\ldots$ $[(1/\varepsilon_{yt})-(1/\varepsilon_{yc})](\varepsilon_1+\varepsilon_2+\varepsilon_3) \geq 1$
ε_{max} (Maximum Principal Strain)	$(\varepsilon_1/\varepsilon_{yt}) \geq 1$ or $(\varepsilon_3/\varepsilon_{yc}) \leq -1$
ε_{eff} (Effective Strain)	$(1/\varepsilon_y)(2U/E)^{½} \geq 1$
γ_{max} (Maximum Shear Strain)	$(\gamma_{max}/\gamma_y) \geq 1$

σ_1, σ_2, and σ_3 are the principal stresses for a given element ($\sigma_1 > \sigma_2 > \sigma_3$), ε_1 , ε_2, and ε_3 are the principal strains for a given element ($\varepsilon_1 > \varepsilon_2 > \varepsilon_3$), γ_{max} is the maximum shear strain, U is the strain energy density, and σ_y, ε_y, and γ_y are the normal failure stress, normal failure strain, and shear failure strain, respectively. CM, H_σ, H_ε, and ε_{max} allow for different tensile (σ_{yt}, ε_{yt}) and compressive (σ_{yc}, ε_{yc}) failure strengths (σ_{yc} and $\varepsilon_{yc} > 0$).

Table 2. Validation parameters as a function of Eqs. (i-iii).

	Eq. (i)	Eq. (ii)	Eq. (iii)
r	0.90	0.86	0.88
Slope	0.94 (CI: 0.82-1.07) [ns]	0.51 (CI: 0.42-0.59) [a]	0.92 (CI: 0.78-1.06) [ns]
Intercept (με)	-31.54 (CI: -77.87-14.79) [ns]	-28.83 (CI: -58.48-0.81) [ns]	-18.32 (CI: -68.74-32.09) [ns]
RMSE (με)	128.59	138.51	130.15
RMSE% [b]	13.17	14.18	13.33
Max err (με)	476.78	750.87	642.82
Max err% [b]	48.82	76.88	65.82

[ns] Not significantly different from 1(slope) or 0 (intercept).

[a] Significantly different from 1 (slope) or 0 (intercept).

[b] Percentage of the maximum absolute measured strain.

FIGURE CAPTIONS

Figure 1. Dorsal, sagittal, and planar views of strain gage rosettes. Three rosettes were mounted distally, immediately proximal to Lister's Tubercle, and three were mounted 3 cm proximal to distal rosettes.

Figure 2. Left – three dimensional illustration of experimental setup. A flat aluminum plate was positioned 60° from vertical (120° as shown here) and brought into contact with the palm of the hand. A second flat aluminum plate was then brought into contact with the dorsal surface of the hand to maintain 60° wrist extension. Right – sagittal view of typical experimental setup.

Figure 3. Left – representative finite element model illustrating surface ρ_{ash} distribution. Top-right – transverse cross sections illustrating internal ρ_{ash} distributions. Bottom-right – Plot of Young's modulus as a function of ρ_{ash} for the three density-elasticity relationships investigated (Eqs. i-iii).

Figure 4. Representative proximal cross sections for two specimens illustrating location of centroid (+), strain gage rosettes (▬), and line of action (●). The wrist joint dislocated during fracture testing for specimen on the right. Note the line of action fell outside the bone cross section for this specimen. The line of action was determined using an unsymmetrical beam theory analysis (See Appendix).

Figure 5. Top – predicted versus measured principal strains at 300 N for Eqs. (i-iii). Bottom – Bland-Altman plots for Eqs. (i-iii). Solid line is the mean difference between predicted and measured strain. Dashed lines are the 95% limits of agreement.

Figure 6. The specimen-mean absolute percent error between experimentally measured and finite element predicted fracture strength as a function of failure theory, tensile-compressive strength ratio *k*, and contiguous volume assumption.

Figure 7. Surface fracture locations of the distal radius vs. finite element failure contours for CM theory, k = 0.5, and volume = 350mm^3. Note that surface elements did not fail (CM failure $\leq$ 1), but displayed higher values at locations where experimental surface fracture was observed.

FIGURES

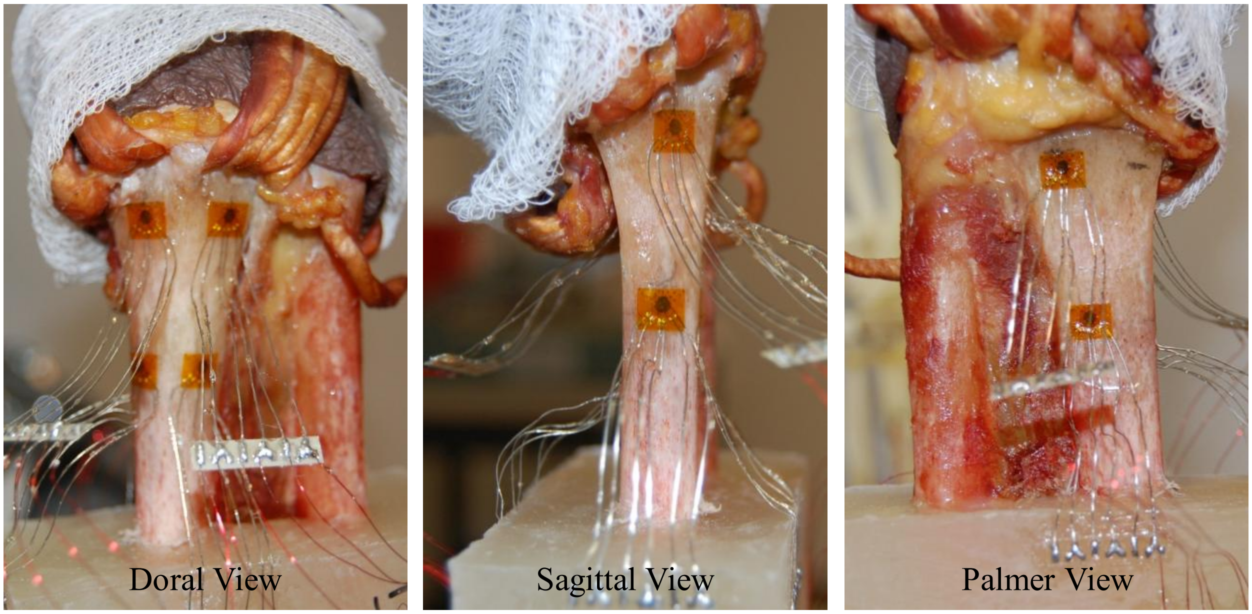

Figure 1.

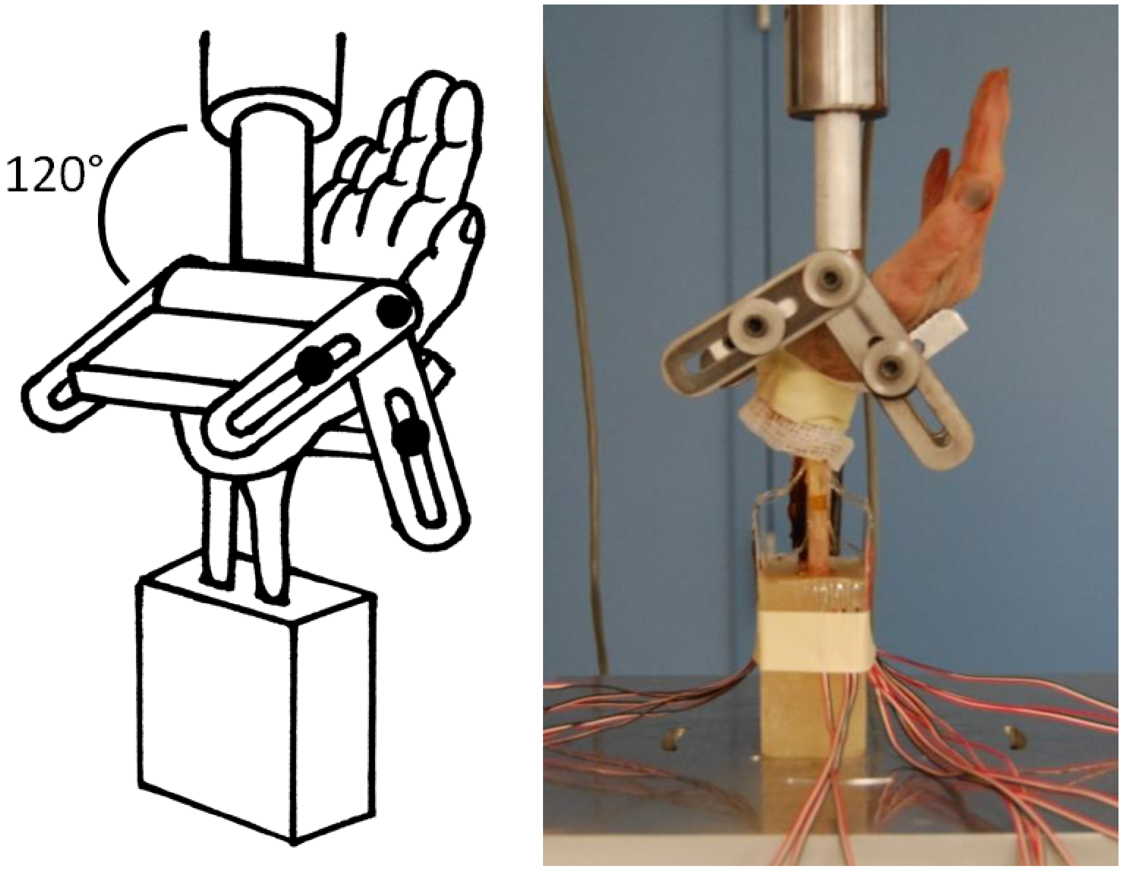

Figure 2.

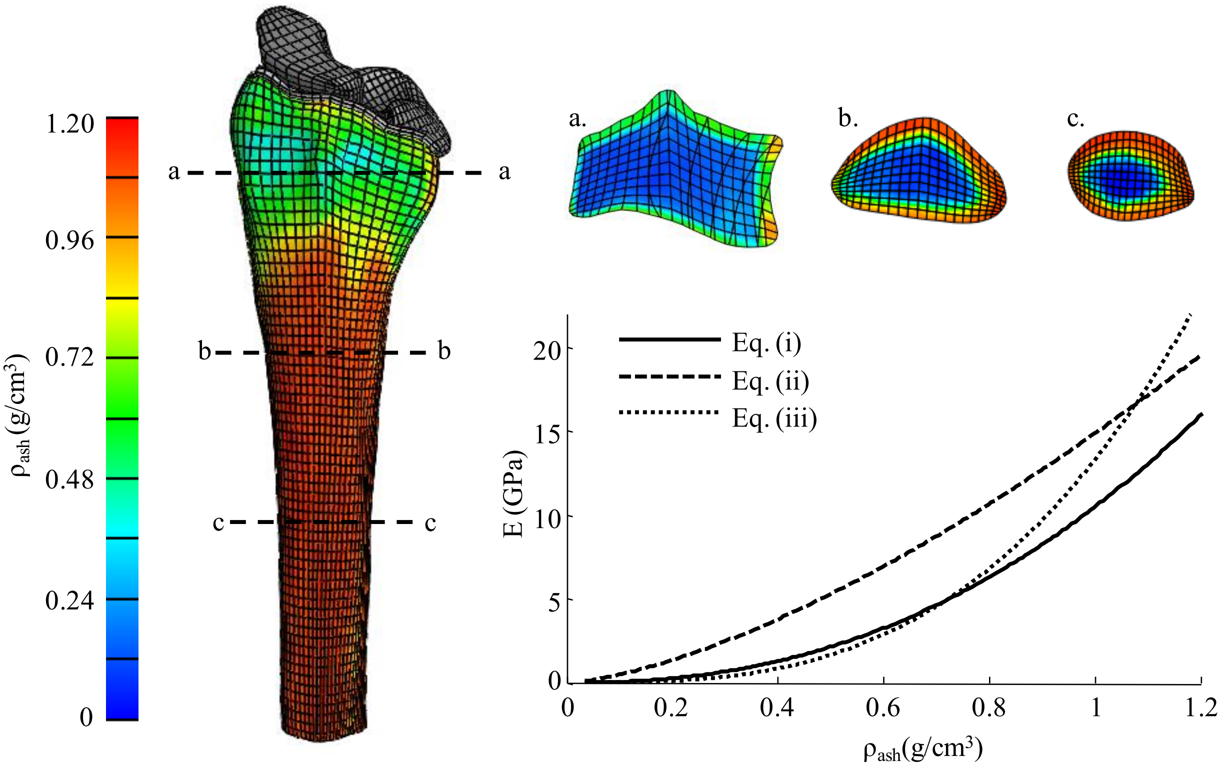

1.20
0.96
0.72
0.48
0.24
0
ρash (g/cm3)
a
a
b
b
c
c
a.
b.
c.
Eq. (i)
Eq. (ii)
Eq. (iii)
E (GPa)
20
15
10
5
0
0
0.2
0.4
0.6
0.8
1
1.2
ρash(g/cm3)

Figure 3.

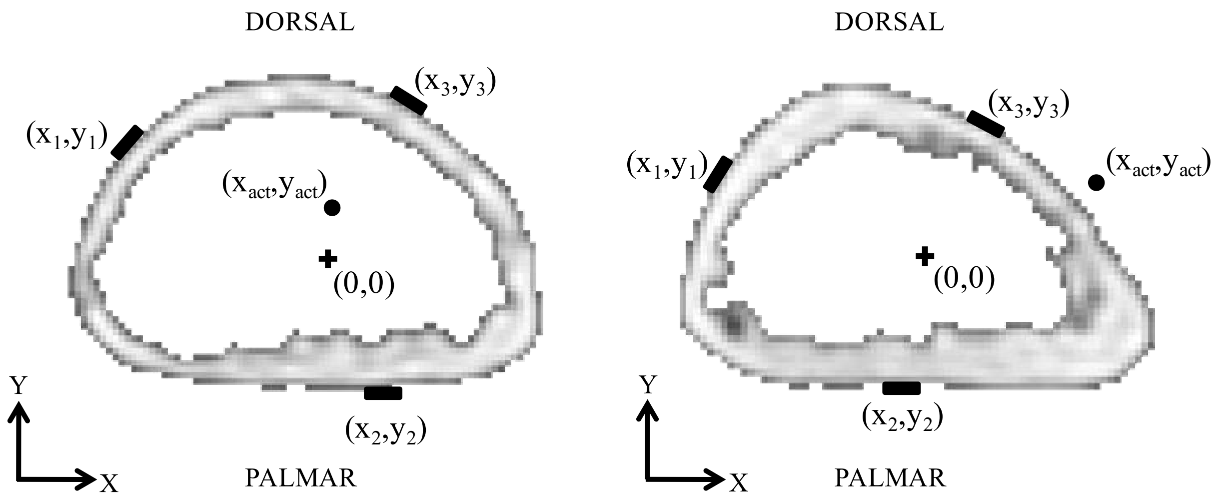
DORSAL
(x_1,y_1)
(x_3,y_3)
(x_{act},y_{act})
$(0,0)$
(x_2,y_2)
PALMAR
Y
X
DORSAL
(x_1,y_1)
(x_3,y_3)
(x_{act},y_{act})
$(0,0)$
(x_2,y_2)
PALMAR
Y
X

Figure 4.

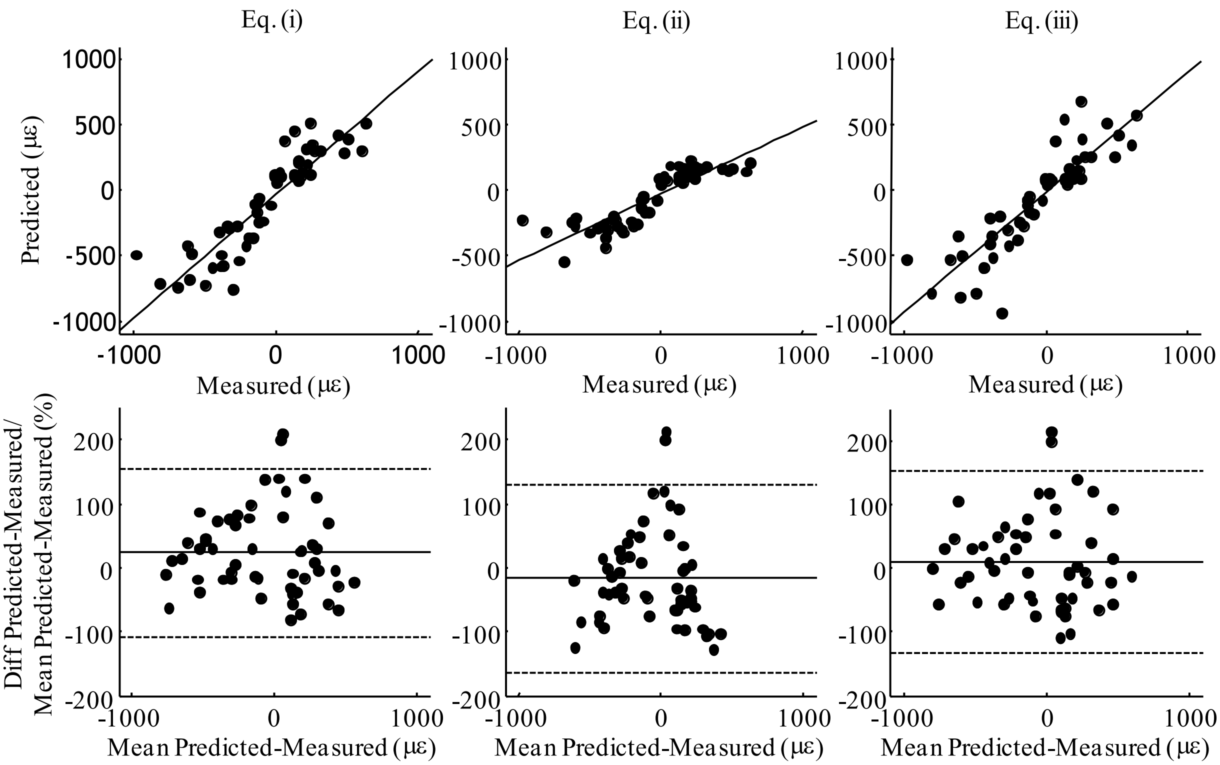
Eq. (i)
Eq. (ii)
Eq. (iii)
Predicted (με)
Measured (με)
Diff Predicted-Measured/
Mean Predicted-Measured (%)
Mean Predicted-Measured (με)
1000
500
0
-500
-1000
200
100
-100
-200

Figure 5.

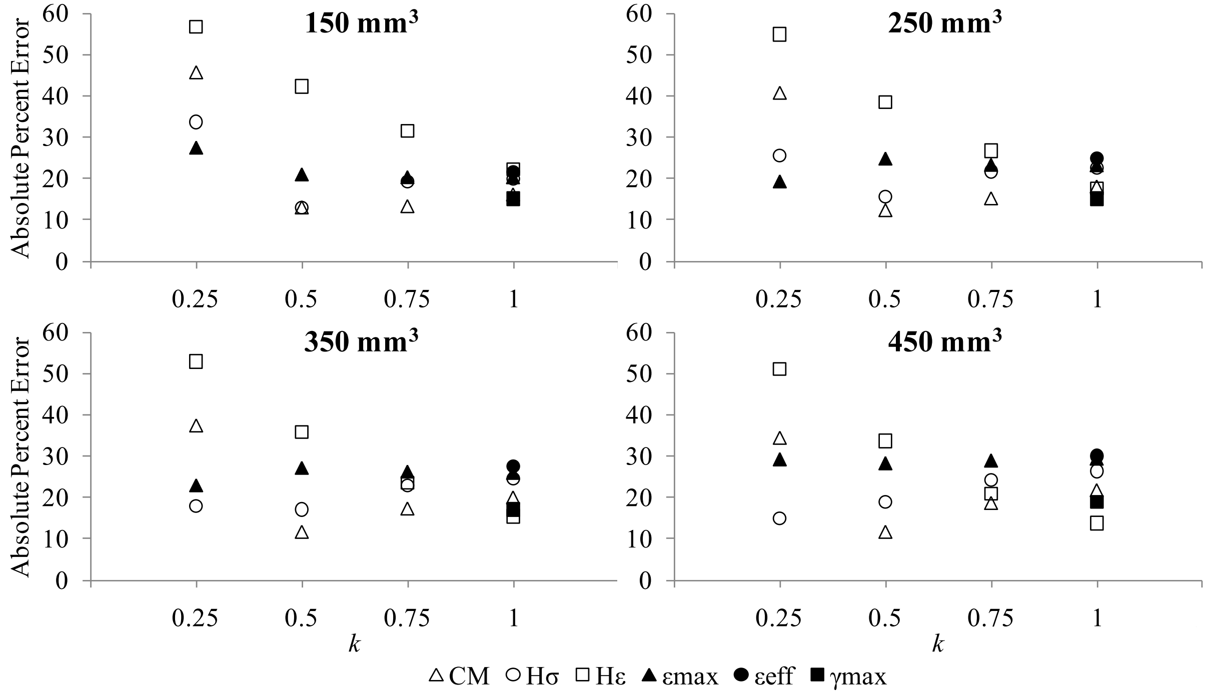

150 mm³
250 mm³
350 mm³
450 mm³
Absolute Percent Error
0
10
20
30
40
50
60
0.25
0.5
0.75
1
k
CM
Hσ
Hε
εmax
εeff
γmax

Figure 6.

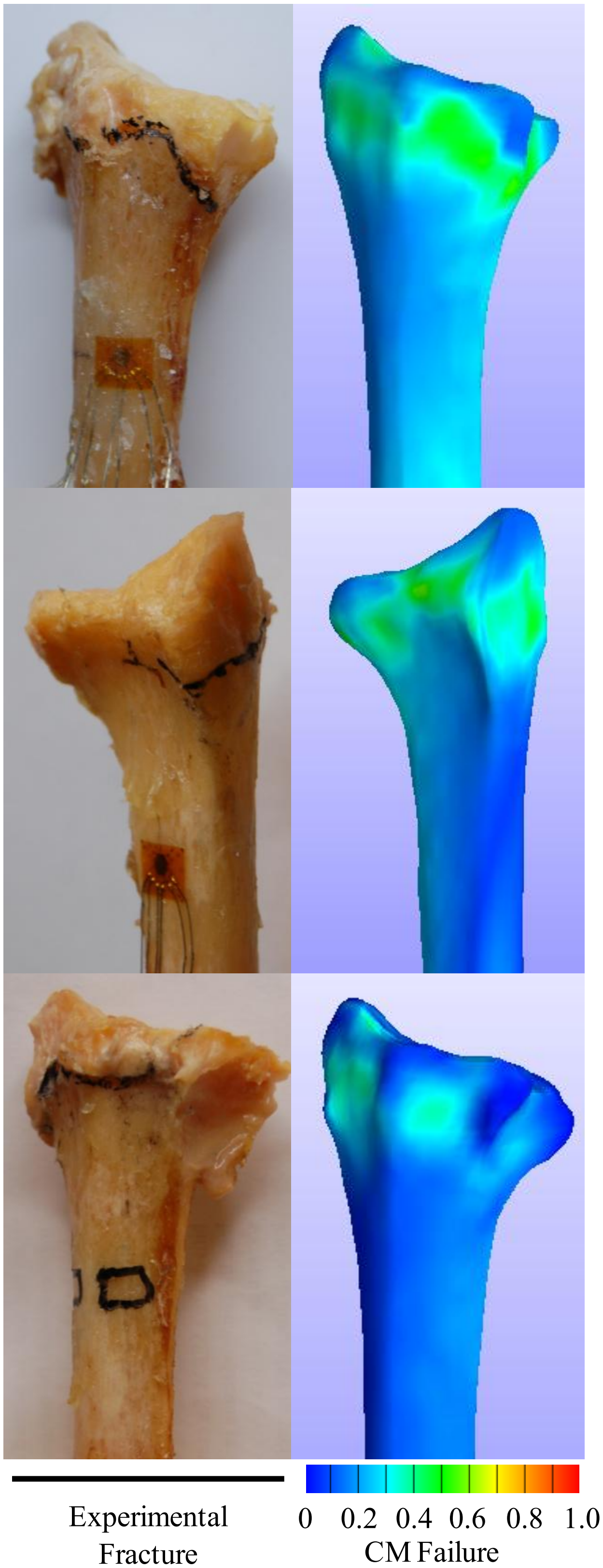

Figure 7.